Plasmonic Oleylamine-Capped Gold and Silver Nanoparticle-Assisted Synthesis of Luminescent Alloyed CdZnSeS Quantum Dots

Plasmonic Oleylamine-Capped Gold and Silver Nanoparticle-Assisted Synthesis of Luminescent Alloyed CdZnSeS Quantum Dots

Oluwasesan Adegoke,*,[†] Kenshin Takemura,[†] and Enoch Y. Park*,[†,‡]

[†]Laboratory of Biotechnology, Research Institute of Green Science and Technology, Shizuoka University, 836 Ohya, Suruga-ku, Shizuoka 422-8529, Japan

[‡]Laboratory of Biotechnology, Department of Bioscience, Graduate School of Science and Technology, Shizuoka University, 836 Ohya, Suruga-ku, Shizuoka 422-8529, Japan

S Supporting Information

ABSTRACT: We report on a novel strategy to tune the structural and optical properties of luminescent alloyed quantum dot (QD) nanocrystals using plasmonic gold (Au) and silver (Ag) nanoparticles (NPs). Alloyed CdZnSeS QDs were synthesized via the organometallic synthetic route with different fabrication strategies that involve alternative utilization of blends of organic surfactants, ligands, capping agents, and plasmonic oleylamine (OLA)-functionalized AuNPs and AgNPs. Ligand exchange with thiol L-cysteine (L-cyst) was used to prepare the hydrophilic nanocrystals. Analysis of the structural properties using powder X-ray diffraction revealed that under the same experimental condition, the plasmonic NPs altered the diffractive crystal structure of the alloyed QDs. Depending on the fabrication strategy, the crystal nature of OLA-AuNP-assisted CdZnSeS QDs was a pure hexagonal wurtzite domain and a cubic zinc-blende domain, whereas the diffraction pattern of OLA-AgNP-assisted CdZnSeS QDs was dominantly a cubic zinc-blende domain. Insights into the growth morphology of the QDs revealed a steady transformation from a heterogeneous growth pattern to a homogenous growth pattern that was strongly influenced by the plasmonic NPs. Tuning the optical properties of the alloyed QDs via plasmonic optical engineering showed that the photoluminescence (PL) quantum yield (QY) of the AuNP-assisted L-cyst-CdZnSeS QDs was tuned from 10 to 31%, whereas the PL QY of the AgNP-assisted L-cyst-CdZnSeS QDs was tuned from 15 to 90%. The low PL QY was associated with the surface defect state, while the remarkably high PL QY exhibited by the AgNP-assisted L-cyst-CdZnSeS QDs lends strong affirmation that the fabrication strategy employed in this work provides a unique opportunity to create single ensemble, multifunctional, highly fluorescent alloyed QDs for tailored biological applications.
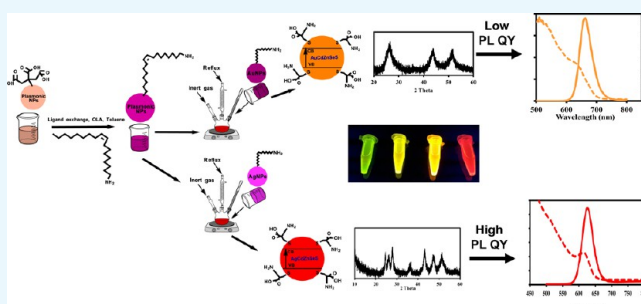
INTRODUCTION

Nanotechnology is a rapidly growing field, and novel nanostructured materials with unique optical properties are needed to meet the demand for the next-generation device materials. Hot-injection organometallic pyrolysis of metal precursors, which is used to produce semiconductor quantum dot (QD) nanocrystals via band gap optical engineering, has become a mainstream fabrication technique to obtain QDs with unique optical properties.[1−3] Fixed metal precursor compositions[4,5] and stoichiometric variations in the metal composition are the two main fabrication techniques used to engineer the band gap of alloyed QDs.[6,7] For the fixed composition technique, a constant molar ratio of the precursor material is usually used to tune the optical properties of the alloyed QDs, whereas for the stoichiometric variation technique, the molar ratio of two or more selected semiconductor metals is varied to tune the optical properties of the resultant alloyed QDs. Both of these techniques have been successfully applied to produce different organic-phase ternary and quaternary alloyed QDs for solar cell applications,[8,9] light-emitting diodes,[10,11] and

optoelectronic applications.[12,13] The choice of the fabrication technique, precursor materials, and semiconductor metal components is an important factor that influences the overall optical properties of the resultant QDs.

Plasmonic optical engineering of QDs has the potential to generate nanostructured materials that can revolutionize research in the fields of medicine, chemistry, biology, photonics, and optoelectronics. For example, embedding QDs on a rough gold film surface generated unique spectral characteristics, an excited-state lifetime that was 1000 times faster, and a 5-fold increase in the photoluminescence (PL) intensity compared to that of the QDs alone.[14−16] Furthermore, plasmonic nanoparticle (NP)-QD core/shell hybrids have been developed for Au−CdSe,[17] Au−ZnS,[18] Au−ZnSe, Au−ZnS/ZnSe, and Au−ZnSe$_x$S$_{1−x}$.[19] The reported Au−ZnSe, Au−ZnS/ZnSe, and Au−ZnSe$_x$S$_{1−x}$ nanostructures[19] were hydrophobic while data on
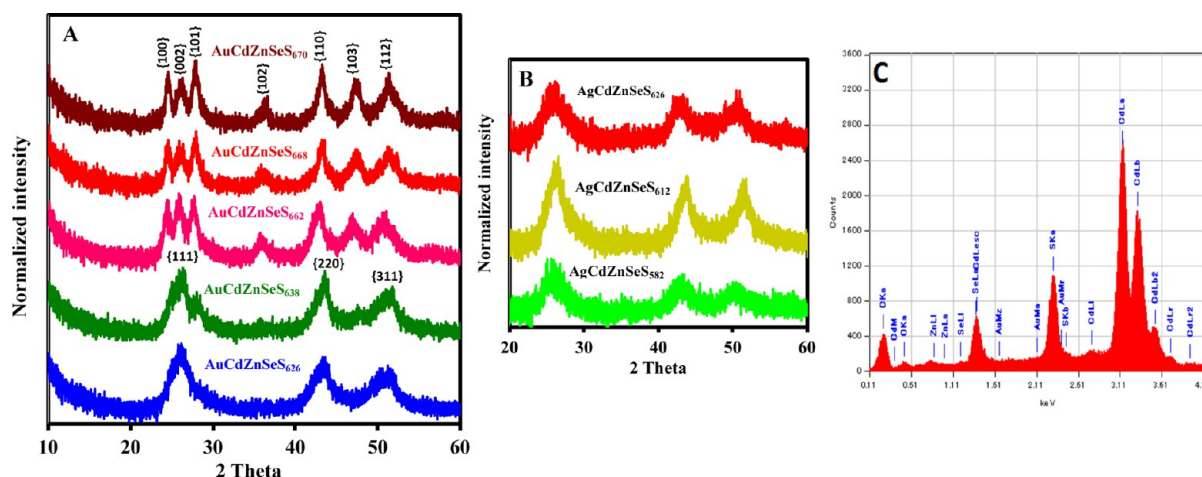
Figure 1. PXRD patterns of the (A) alloyed AuCdZnSeS QDs and (B) alloyed AgCdZnSeS QDs and (C) representative EDX spectrum of the AuCdZnSeS$_{626}$ QDs.

their PL properties were not reported. To date, plasmonic NP-QD core/shell hybrids synthesized via the organometallic hot-injection pyrolysis route have been hydrophobic and have also exhibited poor optical properties because of the plasmonic NPs quenching the fluorescence of the QDs, thus making them unsuitable for biological applications.

Utilizing the precursor solutions of the single ensemble QDs and the plasmonic NPs in the same synthetic pot has been a challenge. Another challenge is preserving the fluorescence of the QDs and generating a high PL quantum yield (QY) after converting the hydrophobic nanocrystals into hydrophilic nanocrystals. A breakthrough report by Jin and Gao[20] demonstrated a layer-by-layer assembly technique to form a single NP ensemble containing the fluorescence of CdSe/ZnS QDs and plasmonic AuNPs. While a relatively moderate PL QY of 18% was reported for the water-soluble plasmonic NP-QD nanostructure, the preparation did not involve pyrolysis of the plasmonic NP and QD metal precursors in the same synthetic pot. The strategy for achieving this feat involves precise optical band gap engineering of the QDs and plasmonic NPs by utilizing appropriate synthetic parameters. In reality, synthesizing discrete fluorescent QD nanocrystals in the quantum confinement regime with unique optical properties using plasmonic NPs as precursors is extremely challenging, and the progress reported to date has either been theoretical[21] or the formation of conjugated nanostructures has resulted in products with insufficient optical properties.[22]

In this work, we report for the first time the organometallic synthetic fabrication of single ensemble fluorescent alloyed QDs assisted with plasmonic NPs. Oleylamine (OLA)-capped AuNPs and AgNPs were synthesized and utilized as precursor materials in a hot-injection organometallic synthetic pot embedded with alternative blends of semiconductor metal precursors, organic capping ligands, and organic surfactants. Then, we converted the hydrophobic alloyed QDs into water-soluble nanocrystals by replacing the organic-capped ligands with hydrophilic L-cysteine (L-cyst) thiol ligands. The structural and optical properties of the optically engineered water-soluble alloyed QDs assisted with plasmonic AuNPs and AgNPs were studied and are reported in this work.

The L-cyst-capped, alloyed CdZnSeS QDs synthesized using the AuNP precursor are denoted as L-cyst-AuCdZnSeS, and those synthesized using the AgNP precursor are denoted as L-cyst-AgCdZnSeS. The samples also have subscripts with the PL emission wavelength to distinguish among the different sizes.

■ RESULTS AND DISCUSSION

Structural Properties. The synthetic strategy employed in this work was used to engineer the band gap of alloyed QDs created using plasmonic NPs as a precursor material and to ascertain how the synthetic process influences the resulting structural features. The powder X-ray diffraction (PXRD) patterns show that the alloyed QDs have well-defined crystalline patterns that depend on the morphology and fabrication method. The cubic zinc-blende crystal structure was observed for the L-cyst-capped AuCdZnSeS$_{626}$, AuCdZnSeS$_{638}$, AgCdZnSeS$_{582}$, AgCdZnSeS$_{612}$, and AgCdZnSeS$_{626}$ QDs (Figure 1A,B). For the zinc-blende AuCdZnSeS$_{626}$ and AuCdZnSeS$_{638}$ QDs, the initial Cd precursor solution with cadmium oxide (CdO), trioctylphosphine oxide (TOPO), octadecene (ODE), and oleic acid (OA) was the same as that used for the synthesis of both QDs, but the ligand hexadeylamine (HDA) was incorporated into the solution for the AuCdZnSeS$_{626}$ QDs. The ligand OLA and the surfactant trioctylphosphine (TOP) were incorporated into the solution for the AuCdZnSeS$_{638}$ QD synthesis. An additional notable difference in the fabrication strategy was the preparation of the TOPSe precursor. The TOPSe precursor for the synthesis of the AuCdZnSeS$_{626}$ QDs was prepared in the presence of the surfactant TOP, and the TOPSe precursor used for the synthesis of the AuCdZnSeS$_{638}$ QDs was prepared in the presence of the surfactants TOPO and TOP and the non-coordinating solvent ODE.

The cubic zinc-blende crystal structure of both sizes of the QDs exhibited three notable peaks with planes at {111}, {220}, and {311}, which demonstrated the strong crystallinity in the alloyed structure. Because the concentration of the plasmonic AuNPs was constant in the synthesis of the alloyed AuCdZnSeS$_{626}$ and AuCdZnSeS$_{638}$ QDs, the synthetic fabrication did not change the crystal phase of the QDs. A different diffraction pattern with respect to the hexagonal wurtzite characteristics was observed when the synthetic fabrication process for the AuCdZnSeS$_{662}$, AuCdZnSeS$_{668}$, and AuCdZnSeS$_{670}$ QDs was tweaked (Figure 1A). The Zn and S precursors were used in a manner similar to that for the synthesis of the AuCdZnSeS$_{626}$ QDs, and the Se precursor was

Table 1. Elemental Composition of the Alloyed L-Cyst-CdZnSeS QDs (with or without Plasmonic NPs as a Precursor Material) Determined via an EDS Analysis

QDs-PL λ (nm)	Cd (%)	Zn (%)	Se (%)	S (%)	C (%)	O (%)
L-cyst-AuCdZnSeS$_{626}$	29.71	1.05	5.61	12.05	43.42	8.16
L-cyst-AuCdZnSeS$_{638}$	24.11	0.06	6.02	13.35	45.96	10.50
L-cyst-AuCdZnSeS$_{662}$	38.6	0.06	13.7	21.61	18.87	7.16
L-cyst-AuCdZnSeS$_{668}$	35.78	0.19	8.32	21.49	24.65	9.58
L-cyst-AuCdZnSeS$_{670}$	12.83	15.23	2.83	9.72	43.41	15.97
L-cyst-AgCdZnSeS$_{582}$	32.76	1.08	12.79	19.16	26.56	8.65
L-cyst-AgCdZnSeS$_{612}$	30.05	1.00	4.62	21.71	31.29	11.32
L-cyst-AgCdZnSeS$_{626}$	25.47	0.73	12.32	14.29	32.05	15.13
L-cyst-CdZnSeS$_{568}$	19.60	0.41	3.29	14.42	47.65	14.63
L-cyst-CdZnSeS$_{586}$	12.80	0.56	7.10	7.04	66.79	5.71
L-cyst-CdZnSeS$_{630}$	36.94	1.48	4.86	27.92	21.25	7.55

used as described for the AuCdZnSeS$_{638}$ QDs. In the initial Cd precursor, the triotylamine (TOA) and tributylphosphine (TBP) precursors, which were not incorporated into the system for the zinc-blende AuCdZnSeS$_{626}$ and AuCdZnSeS$_{638}$ QDs, were added to the synthetic process. An intriguing feature in the diffraction patterns of the AuCdZnSeS$_{662}$, AuCdZnSeS$_{668}$, and AuCdZnSeS$_{670}$ QDs is the absence of a superimposition of the zinc-blende and wurtzite patterns, as a pure hexagonal wurtzite diffraction domain was observed (Figure 1A). The synergistic effect of TOA and TBP along with the plasmonic NP precursor had a profound effect on the phase change in the alloyed QDs.

To determine if the synthetic fabrication method influences the diffraction pattern of the alloyed L-cyst-capped AgCdZnSeS QDs, we utilized the same method used to fabricate the synthesis of the zinc-blende and wurtzite AuCdZnSeS QDs. As shown in Figure 1B, the synthetic method used for the zinc-blende AuCdZnSeS$_{638}$ QDs produced a similar zinc-blende diffraction pattern for the AgCdZnSeS$_{582}$ QDs, and the synthetic method used for the wurtzite AuCdZnSeS QDs produced zinc-blende AgCdZnSeS$_{612}$ and AgCdZnSeS$_{626}$ QDs. This observation shows that the alloyed AgCdZnSeS QDs maintain the same crystallinity regardless of the synthetic process, which is in contrast with the observation for the alloyed AuCdZnSeS QDs. Figure S1 shows a consistent zinc-blende diffraction pattern for the alloyed QDs synthesized without a plasmonic NP precursor when the zinc-blende AuCdZnSeS$_{638}$ fabrication process was employed.

The diffraction pattern was also used to probe the growth of the zinc-blende and wurtzite AuCdZnSeS QDs. A direct correlation between the width of the peak and the growth direction has been proposed by Li and Peng.[23] for zinc-blende CdSe QDs. A sharp peak is attributed to the lateral direction, and a broad peak is attributed to the short axis direction. For the zinc-blende AuCdZnSeS QDs, the sheet thickness corresponded to the [001] direction, and the [001] and {111} directions corresponded to the short axis. The {111} diffraction peak for the AuCdZnSeS$_{638}$ QDs is a superimposition of a sharp peak and a broad peak, which indicated the 2D nature of the structure. Because of the anisotropic nature of the structure, different widths and positions that do not completely overlap are characteristic of the diffraction peaks with lattice planes that correspond to different axial directions.[24] Therefore, the planes in the directions of {100}, {010}, and {110} can be attributed to the lateral growth direction. Because of the asymmetric nature of the wurtzite structure, the growth pattern proposed by Li and Peng cannot

be correlated to the wurtzite structure of the alloyed QDs synthesized in this work. The diffraction pattern simulation by Li and Peng for different orientations of wurtzite 2D CdSe QDs indicated that if the lateral growth is along the [1120] and [0001] axes, the thickness is in the direction of [1010]. Hence, the displayed diffraction pattern exhibited sharp peaks at {002} and {110}. For the wurtzite AuCdZnSeS QDs synthesized in this work, a similar diffraction pattern was observed.

Energy dispersive X-ray spectroscopy (EDS) analysis was carried out to gain useful insight into the elemental compositions of the semiconductor chalcogenide metals, and we have interpreted the result based on the growth rate and the fabrication strategy employed in this study. Table 1 provides the details of the elemental compositions of the alloyed QDs, and Figure 1C shows a representative EDS spectrum of the L-cyst-AuCdZnSeS-QD$_{626}$, and Figure S2 shows the elemental mapping images of Cd, Zn, Se, and S metal chalcogenide for wurtzite AuCdZnSeS and zinc-blende AgCdZnSeS QDs. On the basis of the fabrication strategy used to generate the wurtzite diffraction pattern for AuCdZnSeS QDs, the comparison of the elemental composition of L-cyst-AuCdZnSeS$_{662}$, L-cyst-AuCdZnSeS$_{668}$, and L-cyst-AuCdZnSeS$_{670}$ QDs unraveled a steady decrease in the Cd, Se, and S composition, while the Zn composition increased relative to the particle size increase. The metal composition trend obtained for AgCdZnSeS QDs shows that on the basis of the fabrication strategy used to tune the size of the QDs, both the Cd and Zn composition decreased as the size of the QDs increased, whereas the Se and S composition showed no noticeable trend relative to the particle size. For the CdZnSeS QDs synthesized without plasmonic NPs, the Zn content increased relative to increase in the size of the QDs, whereas there was no noticeable trend in the Cd, Se, and S content relative to the particle size of the nanocrystal.

With respect to how the elemental composition can be used to understand the growth rate of the QDs, one can see that the Cd content of L-cyst-AuCdZnSeS$_{662}$, L-cyst-AuCdZnSeS$_{668}$, and L-cyst-AuCdZnSeS$_{670}$ synthesized from the same batch shows a Cd-rich alloyed system which depleted as the size of the QDs grew. It implies that for wurtzite AuCdZnSeS QDs, the depletion of the Cd-rich system with time in relation to the particle size increase correlated conversely to a gradual formation of a Zn-rich system, whereas for the zinc-blende AgCdZnSeS QDs, the depletion of the Cd-rich system correlated precisely to the depletion of the Zn-rich system.

To probe the particle morphology of the alloyed QDs, we carried out a transmission electron microscopy (TEM) analysis.
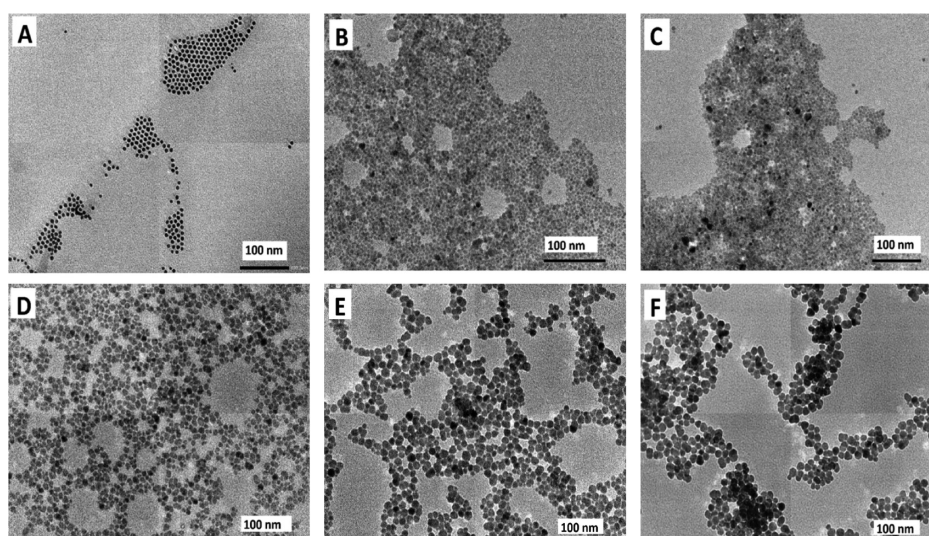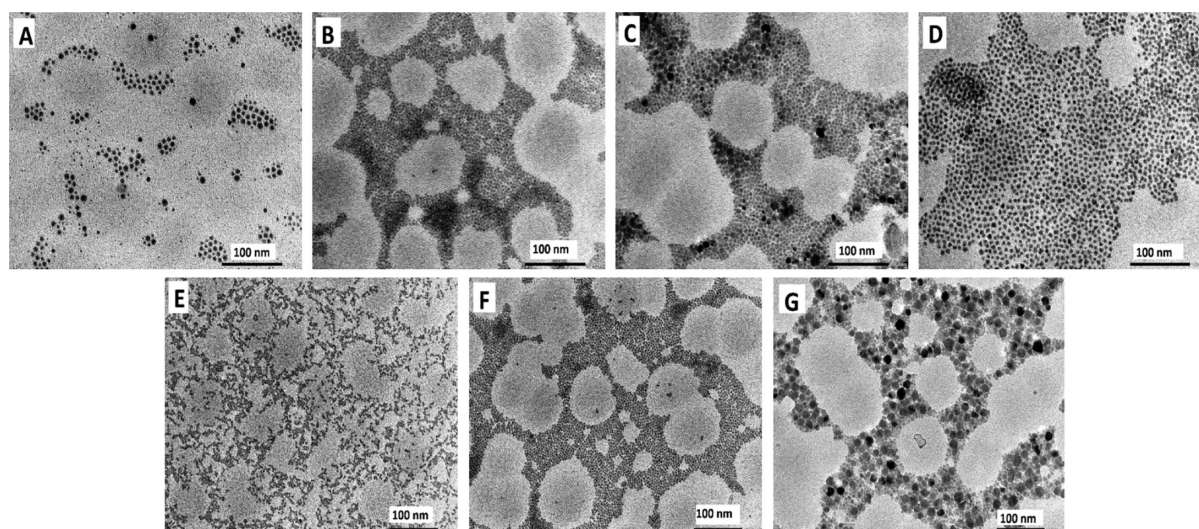
Figure 2. TEM images of the (A) OLA-AuNPs, (B) L-cyst-AuCdZnSeS-QD$_{626}$, (C) L-cyst-AuCdZnSeS-QD$_{638}$, (D) L-cyst-AuCdZnSeS-QD$_{662}$, (E) L-cyst-AuCdZnSeS-QD$_{668}$, and (F) L-cyst-AuCdZnSeS-QD$_{670}$.

Table 2. Summary of the Morphological Size, Hydrodynamic Size, ZP, and Photophysical Properties of the Size-Dependent, Alloyed L-Cyst-CdZnSeS QDs Synthesized with or without Plasmonic NPs as a Precursor Material

QDs-PL λ (nm)	λ_{Abs} (nm)	fwhm (nm)	TEM (nm)	DLS (nm)	ZP (mV)	PL QY (%)
L-cyst-AuCdZnSeS$_{626}$	596	48	3.4 ± 1.2	7.9 ± 2.1	−49.6 ± 7.5	16
L-cyst-AuCdZnSeS$_{638}$	612	46	3.7 ± 1.4	9.1 ± 2.8	−69.1 ± 8.1	22
L-cyst-AuCdZnSeS$_{662}$	640	46	5.3 ± 3.2	10.8 ± 3.3	−57.5 ± 7.6	31
L-cyst-AuCdZnSeS$_{668}$	640	40	6.1 ± 1.4	19.1 ± 5.7	−38.2 ± 4.3	13
L-cyst-AuCdZnSeS$_{670}$	642	42	7.0 ± 1.4	55.8 ± 22.4	−41.8 ± 7.8	10
L-cyst-AgCdZnSeS$_{582}$	554	46	2.5 ± 0.5	4.7 ± 1.0	−48.6 ± 6.1	15
L-cyst-AgCdZnSeS$_{612}$	576	56	3.7 ± 1.7	6.0 ± 1.8	−52.2 ± 4.2	90
L-cyst-AgCdZnSeS$_{626}$	610	38	4.1 ± 1.8	7.6 ± 1.6	−46.8 ± 6.0	49
L-cyst-CdZnSeS$_{568}$	552	42	3.0 ± 0.8	2.2 ± 0.6	−45.9 ± 5.0	15
L-cyst-CdZnSeS$_{586}$	574	46	3.2 ± 0.7	6.9 ± 1.7	−38.4 ± 4.7	18
L-cyst-CdZnSeS$_{630}$	584	48	∼4.0 ± 2.5	15.9 ± 4.5	−55.0 ± 5.8	84

Figure 3. TEM images of the (A) OLA-AgNPs, (B) L-cyst-AgCdZnSeS-QD$_{582}$, (C) L-cyst-AgCdZnSeS-QD$_{612}$, (D) L-cyst-AgCdZnSeS-QD$_{626}$, (E) L-cyst-CdZnSeS-QD$_{568}$, (F) L-cyst-CdZnSeS-QD$_{586}$ and (G) L-cyst-CdZnSeS-QD$_{630}$.

Figure 2 shows the representative TEM images of OLA-AuNPs and the alloyed AuCdZnSeS QDs, whereas Table 2 provides details on the average particle size. Figure 2A shows that the OLA-AuNPs exhibited spherical, homogenous particle mor-phology, as evident by their monodispersed nature. The average particle size distribution, as shown in Figure 2A, was 5.0 ± 2.1. Figure 2B−F shows the representative TEM images of the different-sized AuCdZnSeS QDs that were synthesized using
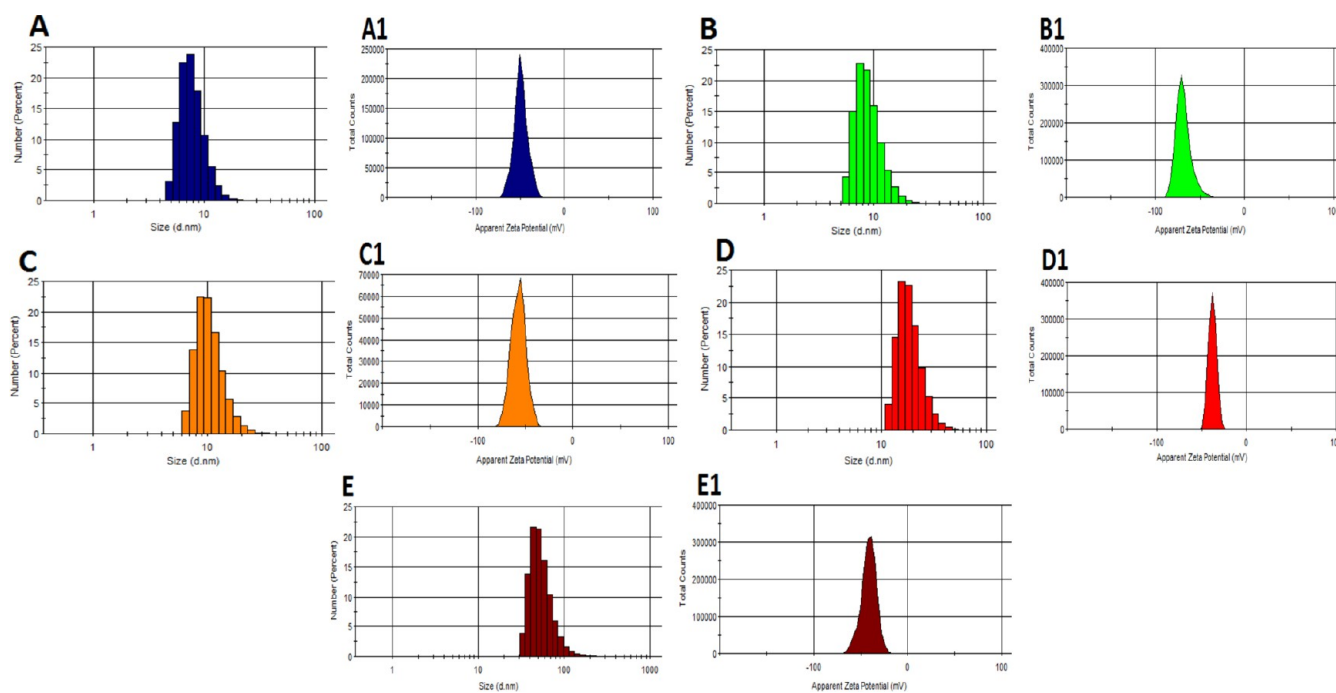
Figure 4. DLS and ZP curves for the (A,A1) L-cyst-AuCdZnSeS-QD$_{626}$, (B,B1) L-cyst-AuCdZnSeS-QD$_{638}$, (C,C1) L-cyst-AuCdZnSeS-QD$_{662}$, (D,D1) L-cyst-AuCdZnSeS-QD$_{668}$, and (E,E1) L-cyst-AuCdZnSeS-QD$_{670}$.

OLA-AuNPs as the precursor. As the QDs increased in size, the particle morphology transitioned from a heterogeneous nucleation state to a homogenous nucleation state. The spherical particle morphologies of the L-cyst-AuCdZnSeS$_{662}$ (Figure 2D), L-cyst-AuCdZnSeS$_{668}$ (Figure 2E), and L-cyst-AuCdZnSeS$_{670}$ QDs (Figure 2F) exhibited improved particle dispersity compared with those of the L-cyst-AuCdZnSeS$_{626}$ (Figure 2B) and L-cyst-AuCdZnSeS$_{638}$ QDs (Figure 2C). Figure S3 shows the corresponding particle size distribution histograms, which reflect the progressive increase in the particle size (Table 2) as the alloyed QDs were subjected to further growth.

The OLA-AgNPs (Figure 3A), which were used as a precursor to synthesize the AgCdZnSeS QDs, had a particle size of 3.3 ± 1.7 and a spherical, monodispersed particle distribution. A closer look at the TEM images of the AgCdZnSeS QDs (Figure 3B−D) and AuCdZnSeS QDs (Figure 2B−F) shows that the smaller, alloyed QDs exhibited prolate heterogeneous particle morphologies that correlated to the anisotropic growth[25] and progressively changed into a homogenous particle morphology as the particle growth time increased. Interestingly, this transitional feature of the particle morphology was not observed in the TEM images of the alloyed QDs (Figure 3E,F) that were synthesized without plasmonic NPs. An additional feature is the distinct spherical shape morphology of the alloyed QDs with precursor plasmonic NPs compared with that of the alloyed QDs without precursor plasmonic NPs. The corresponding particle size distribution histograms for the alloyed AgCdZnSeS QDs are shown in Figure S4, whereas those of the alloyed CdZnSeS QDs are shown in Figure S5.

The heterogeneous anisotropic growth in the smaller-sized QDs with precursor plasmonic NPs can be understood in terms of the slow reactivity of the NPs and the low reaction temperature. This implies that at lower reaction temperature (typically 200−240 °C), the slow reactivity of the NPs would

have prevented the uniform formation of the QD nuclei throughout the entire synthetic solution. The heteroepitaxial growth of the alloyed QDs under these conditions is kinetically controlled and slow; that is, the rate-limiting step is the formation of CdZnSeS at the surface along with the diffusion of the NPs. Therefore, the wurtzite AuCdZnSeS QDs with homogenous nucleation and growth do not favor anisotropic-type growth.

Photon correlation spectroscopy or quasi-elastic light scattering, that is, dynamic light scattering (DLS), was used to probe the hydrodynamic sizes of the QDs in solution. The hydrodynamic size value was used as a reference to probe the aggregation state of the nanocrystals. If the alloyed QDs are polydispersed in a solution, the hydrodynamic size will be larger than 100 nm. For a monodispersed colloidal solution, the hydrodynamic size should be smaller than 100 nm. The DLS curves for the different-sized, alloyed AuCdZnSeS QDs are shown in Figure 4A−E, and those for the AgCdZnSeS QDs and CdZnSeS QDs are shown in Figures S6A−C and S7A−C, respectively. The monodispersed nature of the colloidal QD solutions was confirmed by their hydrodynamic size values, which were smaller than 100 nm (Table 2).

The colloidal stability of the alloyed QDs was measured using the zeta potential (ZP) curves of the alloyed QDs, as shown in Figure 4A1−E1 for the AuCdZnSeS QDs, in Figure S6A1−C1 for the AgCdZnSeS QDs, and in Figure S7A1−C1 for the CdZnSeS QDs. A high colloidal stability is indicated by a ZP value in the range of ±30 mV. Each of the alloyed QDs grown with plasmonic NPs exhibited a high colloidal stability based on the ZP values (Table 2), which were in the range of −38.2 to −69.1 mV. The alloyed QDs grown without plasmonic NPs also exhibited a high colloidal stability. The precursor plasmonic NPs used in the synthetic fabrication of the QDs did not alter the colloidal stability of the resulting nanocrystals.
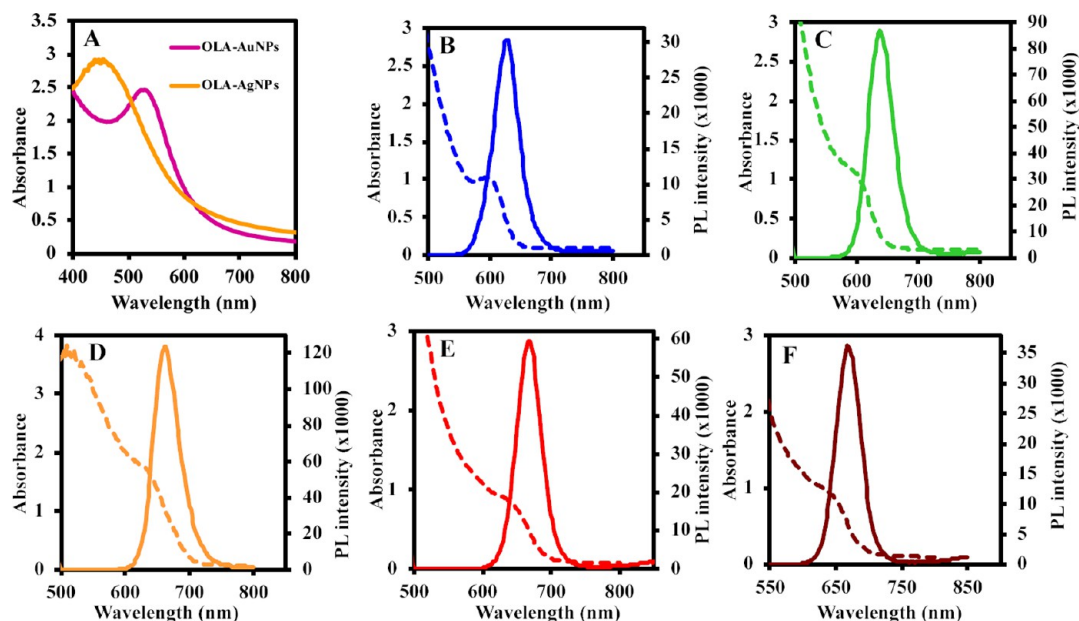
Figure 5. UV/vis absorption spectra of the (A) OLA-AuNPs and OLA-AgNPs. UV/vis absorption and fluorescence emission spectra of the (B) L-cyst-AuCdZnSeS-QD$_{626}$, (C) L-cyst-AuCdZnSeS-QD$_{638}$, (D) L-cyst-AuCdZnSeS-QD$_{662}$, (E) L-cyst-AuCdZnSeS-QD$_{668}$, and (F) L-cyst-AuCdZnSeS-QD$_{670}$.
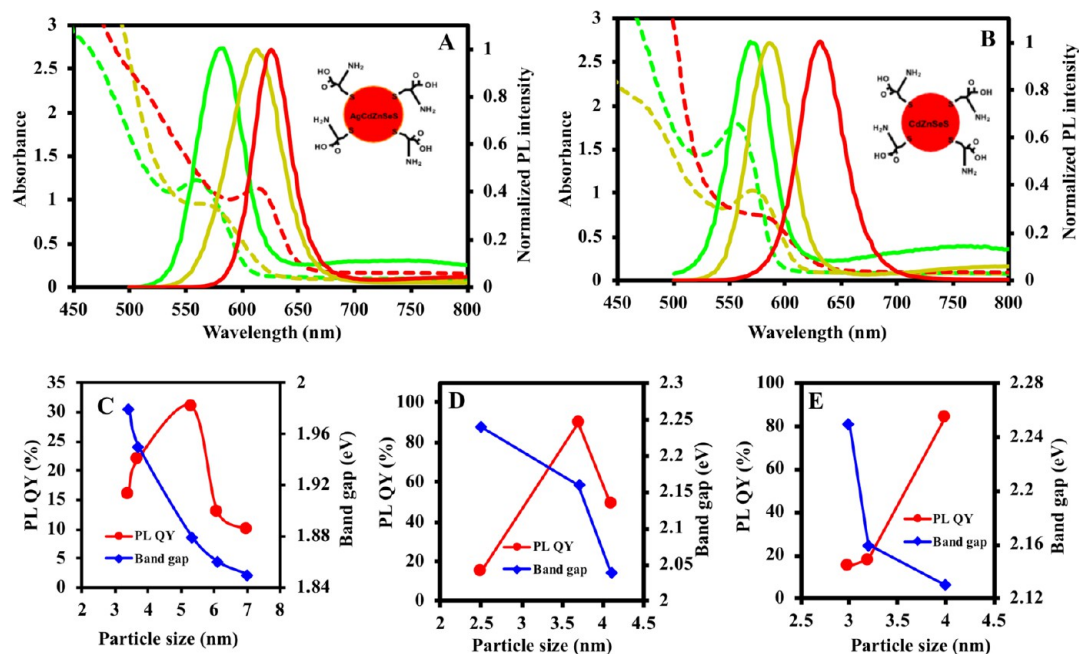
Figure 6. UV/vis absorption and fluorescence emission spectra of the (A) L-cyst-AgCdZnSeS QDs and (B) CdZnSeS QDs (without a plasmonic NP precursor). PL QY and a function of the band gap for the (C) L-cyst-AuCdZnSeS QDs, (D) L-cyst-AgCdZnSeS QDs, and (E) CdZnSeS QDs (without a plasmonic NP precursor).

Optical Properties. The UV/vis absorption spectra of the OLA-AuNPs and OLA-AgNPs are shown in Figure 5A. The surface plasmon resonance (SPR) peak, which was narrower for the OLA-AuNPs, absorbed at ∼530 nm, and a much broader SPR peak, which absorbed in the range of 438−456 nm, was observed for the OLA-AgNPs. The UV/vis absorption and PL emissions of the different-sized alloyed AuCdZnSeS QDs are shown in Figure 5B−F, and a summary of the photophysical parameters, that is, the absorption maximum wavelength, full width at half maximum (fwhm), and PL QY, is shown in Table 2. To calculate the PL QY of the QDs, rhodamine 6G was

dissolved in ethanol and used as a reference standard (Φ_{Fl}^{R6G} = 0.95).[26] The equation below was used to evaluate the PL QY of the alloyed QDs

$$\Phi_{Fl}^{QD} = \Phi_{Fl}^{R6G} \frac{F_1^{QD} \cdot OD_{R6G_{(\lambda exc)}} \cdot n_{water}^2}{F_1^{R6G} \cdot OD_{QD_{(\lambda exc)}} \cdot n_{ethanol}^2}$$

Φ_{Fl}^{QD} is the PL QY of the alloyed QDs, Φ_{Fl}^{R6G} is the PL QY of the rhodamine 6G standard, F_1^{QD} and F_1^{R6G} are the sums of the fluorescence intensities of the QDs and rhodamine 6G standard, respectively, $OD_{QD_{(\lambda exc)}}$ and $OD_{R6G_{(\lambda exc)}}$ are the optical

densities of the QDs and the standard at the wavelength of excitation, respectively, and $n_{ethanol}^2$ and n_{water}^2 are the refractive indexes of the solvent used to dissolve the standard and QDs, respectively.

The red-shifted PL emission of the wurtzite AuCdZnSeS QDs within the range of 626−670 nm is an indication of exciton delocalization over the entire metal semiconductor chalcogenide because of the synergistic effect of the precursor materials. The UV/vis absorption spectra for the AuCdZnSeS QDs showed that the excitonic absorption peak for the L-cyst-AuCdZnSeS$_{626}$ QDs was much narrower than that for the other alloyed AuQDs. This can be attributed to an increase in the growth time for the alloyed QDs rather than an increase in the quality of the surface. Additionally, the fwhm of the AuCdZnSeS$_{626}$ (48 nm) QDs was slightly larger than that of the other alloyed QDs.

To understand how the synthetic method influences the optical properties of the different-sized, alloyed AuCdZnSeS QDs, an assessment of the fwhm and the PL QY parameters was performed. Generally, a lower fwhm and a higher PL QY indicate QDs with fewer surface defects and vice versa. On the basis of a comparison of the fwhm and PL QY values (Table 2), the AuCdZnSeS$_{668}$ QDs had the lowest fwhm and a relatively low PL QY (13%), whereas the AuCdZnSeS$_{662}$ QDs had a much higher fwhm and the highest PL QY. Additionally, we determined that an increase in the particle size of the wurtzite AuCdZnSeS QDs correlated to a spontaneous decrease in the PL QY. An intriguing observation was the remarkable PL QY of 90% and the corresponding fwhm of 56 nm exhibited by AgCdZnSeS$_{612}$ QDs. On the basis of this assessment, a direct relationship between the fwhm and the PL QY does not exist for the alloyed QDs.

The UV/vis absorption and PL emission spectra of the AgCdZnSeS QDs are shown in Figure 6A, which clearly reveal the presence of a deep trap emission in the tail end of the PL emission peak; they followed the order of AgCdZnSeS$_{582}$ > AgCdZnSeS$_{626}$ > AgCdZnSeS$_{612}$. The extent of the deep trap PL emission is reflected in the resulting PL QY and depicts the surface defect level in the alloyed nanocrystals. A similar observation in the deep trap emission was also observed for the alloyed CdZnSeS QDs synthesized without the plasmonic NPs (Figure 6B). On the basis of an assessment of the tail end of the PL emission peak of the CdZnSeS QDs, the extent of the deep trap emission followed the order of CdZnSeS$_{568}$ > CdZnSeS$_{586}$ > CdZnSeS$_{630}$, and this precisely correlated with the resulting trend in the PL QY. The plots of the particle size as a function of the band gap and PL QY for the L-cyst-AuCdZnSeS, AgCdZnSeS and CdZnSeS QDs are shown in Figure 6C−E. Because the band gaps of the alloyed AuCdZnSeS and AgCdZnSeS QDs were tuned by the nature of the precursor materials, the results show that the resulting photophysical properties are largely affected by the synthetic method. The lower PL QY may be due to the inherent presence of residual strain within the nanocrystal interface, which may be due to a lattice mismatch between the semiconductor metal components, whereas the higher PL QY may be due to relaxation of the strain and radiative exciton recombination within the alloyed nanocrystals.

Viability Assay. The popular methyl thiazolyl tetrazolium bromide (MTT) assay[27] was used to evaluate the cytotoxicity of the alloyed QDs. The cell assay method was carried out according to a previously published protocol by our group.[28] Figure S8A−C shows the cytotoxicity responses of selected L-cyst-CdZnSeS$_{630}$, L-cyst-AuCdZnSeS$_{662}$, and L-cyst-AgCdZnSeS$_{612}$ QDs to HEK 296T cells. The alloyed QDs with a high PL QY were selected for the cytotoxicity assay. For the L-cyst-CdZnSeS$_{630}$ QDs (Figure S8A) synthesized without plasmonic NPs, an excellent cell viability was observed at both low and high dose levels with the exception of 1 μg/mL. For the AuCdZnSeS$_{662}$ QDs, excellent cell viability was observed at dose concentrations of 1 mg/mL, 1 μg/mL, and 0.1 ng/mL, and for the AgCdZnSeS$_{612}$ QDs, excellent cell viability was observed at dose concentrations of 1 mg/mL, 0.1 mg/mL, and 0.1 μg/mL. Generally, a cell viability trend that correlated to the concentration of the QDs was not observed.

Mechanism of Plasmon-Assisted QD Growth. To understand the growth mechanism of the plasmonic AuNP and AgNP-assisted synthesis of CdZnSeS QDs with respect to transition in the morphological growth of the particle from a heterogeneous state to a homogenous state, we have utilized the LaMer mechanism, the Ostwald ripening, and digestive ripening for illustration.[29] The LaMer mechanism involves a two-stage conceptual process of nucleation and growth separation and can be divided into three stages: (1) increase in the free monomer concentration occurs rapidly in solution; (2) the concentration of the free monomer in solution is significantly reduced because of burst nucleation. At this stage, the rate of nucleation is ascribed as effectively infinite in which no nucleation occurs after this period because of the depletion in the concentration of the monomer; (3) after the nucleation process, the diffusion of the monomer through the solution triggers the growth.[30]

For Ostwald ripening, the growth mechanism is triggered by the change in the solubility of the nanocrystal which is dependent on the QDs size. Hence, as a result of the surface energy and high solubility of smaller particles in solution, the particles redissolve, and this in turn enables the growth of larger particles. On the other hand, digestive ripening is the inverse of Ostwald ripening in which smaller particles grow at the expense of larger particles. This growth process is also controlled by surface energy of the particles in solution by which larger particles redissolve to in turn allow smaller particles to grow.[31]

Considering the three mechanisms presented, we can tentatively eliminate the digestive ripening growth process for the plasmon-assisted QDs synthesis because the QD nucleation and growth led to increase in the particle size, thus leaving us with the LaMer mechanism and Ostwald ripening mechanism. The study of the excitonic absorption spectra of the QDs using UV/vis spectroscopy can shed light on the nature of the nucleation and growth mechanism of the QDs considering the influence of temperature on growth. For AgCdZnSeS QDs, the smaller-sized QDs were obtained at a lower temperature and shorter time as compared to the larger-sized QDs which were harvested at longer time and higher temperature. The corresponding UV/vis absorption spectra reveal a slight broadening of the maximum excitonic absorption peak as the size of the QDs increased. This growth process fits strongly to the Ostwald ripening mechanism. For AuCdZnSeS QDs, the monomer effect seems to play a major role on the nucleation and growth of the nanocrystals because of the exhibited differences in the diffraction pattern when different fabricated strategies were employed. We envisage that the phosphonic precursor materials can deoxygenate the AuNP precursor and the OA or the other capping ligands to generate anhydride products.[32] We envision that at relatively high temperature (between 220 and 240 °C), the particles formed by LaMer

Scheme 1. Schematic Representation of the Synthetic Process for the Zinc-Blende and Wurtzite, Alloyed CdZnSeS QDs with Plasmonic NP Precursors. Emission Colors of the Alloyed QDs under UV Irradiation
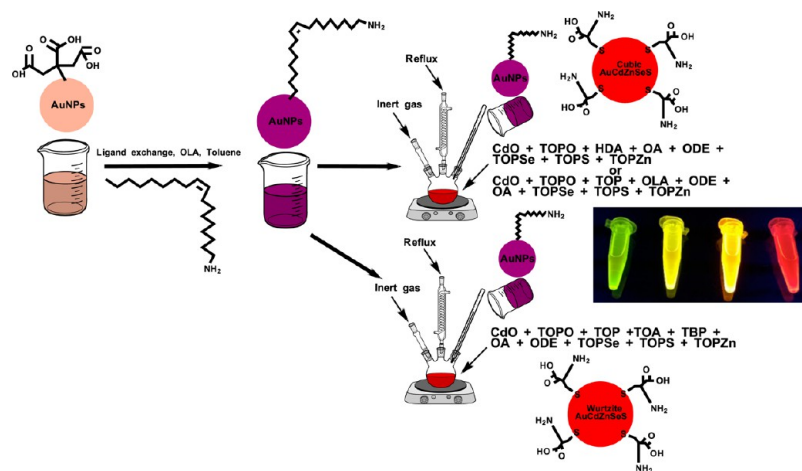
burst nucleation which was followed by rapid random attachment and by intraparticle ripening, hence leading to a heterogeneous particle morphology. At very high temperatures (>280 °C), the particle undergoes a much longer nucleation which was followed by slow growth, hence leading to a homogeneous particle morphology.

Further Discussion on the PL QY. Exploring the different fabrication strategies, we tuned the PL QY of AuCdZnSeS QDs to a maximum value of 31% and AgCdZnSeS QDs to a maximum value of 90%. We believe that there are a number of reasons for the significant differences in the PL QY. From the UV/vis absorption spectra of the different-sized AuCdZnSeS (Figure 5B−F) and AgCdZnSeS QDs (Figure 6A), it is evident that the SPR peak of the plasmonic NPs were buried under the strong excitonic absorption peak of the QDs. The vital question is whether the utilization of the plasmonic NPs as a precursor material will induce a radiative or nonradiative fluorescent state in the QDs. A key characteristic to note is that Au nanostructures are well-known fluorescence quenchers, and their presence within fluorescent materials can inhibit photon transmittance.[33] Because the PL QY of CdZnSeS QDs synthesized without plasmonic NPs reached a maximum of 84%, it implies that the presence of AuNP precursors in the synthetic process influenced the low PL QY. One possible reason for this is that the Au^{3+} may have etched onto the QD surface and introduced surface traps which suppressed the radiative exciton recombination state of the QDs.

For AgCdZnSeS QDs which exhibited a remarkable PL QY, we envision that the Ag^+ had less accessibility to the QD surface, thus allowing for more radiative exciton recombination states. Another possible reason for the differences in the PL QY may be the extent of spacing between the spectral overlap of the QDs fluorescence and the SPR absorption peak of the plasmonic NPs. As shown in Figure 5A, the SPR peak of OLA-AgNPs absorbs between 438 and 456 nm, whereas that of OLA-AuNPs absorbs at ~530 nm. We can tentatively conclude that the significant overlap and the short separation distance between the AuNP SPR peak and the QDs fluorescence suppressed the radiative exciton recombination state in the resulting AuCdZnSeS QDs, whereas longer overlap and longer separation distance between the AgNP SPR peak and the QDs fluorescence favored radiative exciton recombination states in the resulting AgCdZnSeS QDs.

CONCLUSIONS

In this work, we successfully engineered for the first time the band gap of alloyed quaternary CdZnSeS QDs with plasmonic NPs in an organometallic synthetic pot embedded with organic surfactants and coordinating ligands. The influence of the plasmonic NP precursor on the QD growth morphology revealed a steady transition from a heterogeneous growth pattern to a homogeneous growth pattern. Such a growth pattern was not evident in the particle morphology of alloyed QDs synthesized without plasmonic NP precursors. A strong structural influence was unraveled in the crystal nature of the plasmonic NP-assisted alloyed QDs, with results showing that under the same experimental conditions, the alloyed QDs synthesized with plasmonic OLA-AgNPs exhibited a hexagonal wurtzite structure, whereas the alloyed QDs synthesized with OLA-AuNPs exhibited a cubic zinc-blende structure. A detailed analysis of the optical properties indicated that the band gap of the plasmonic NP-assisted alloyed QDs can be tuned across the visible region to the near-infrared region. The variations in the PL QY lend strong evidence that depending on the fabrication strategy and the nature of the plasmonic NP being utilized, the alloyed QDs can attain a high radiative recombination exciton state that correlates to a high PL QY.

EXPERIMENTAL METHODS

Materials. Cadmium oxide (CdO), TOP, ODE, HDA, TOPO, selenium (Se), TOA, TBP, diethylzinc (Et_2Zn), sulfur (S), OLA, rhodamine 6G, *N*-(3-dimethylaminopropyl)-*N'*-ethylcarbodiimide hydrochloride, *N*-hydroxysuccinimide, $HAuCl_4·3H_2O$, tannic acid, silver nitrate ($AgNO_3$), and L-cysteine were purchased from Sigma-Aldrich Co. LLC (Saint Louis, MO, USA). OA was purchased from Nacalai Tesque Inc. (Kyoto, Japan). Potassium hydroxide (KOH), methanol, trisodium citrate, acetone, and chloroform were purchased from Wako Pure Chemical Ind., Ltd. (Osaka, Japan). An ultrapure Milli-Q water system was used for the sample preparation.

Characterization. UV/vis absorption and fluorescence emission measurements were performed using a filter-based multimode microplate reader (Infinite F500, Tecan, Ltd., Männedorf, Switzerland). TEM images were obtained using TEM JEM-2100F (JEOL, Ltd., Tokyo, Japan) operated at 100 kV. PXRD measurements were carried out using RINT Ultima XRD (Rigaku Co., Tokyo, Japan) with an Ni filter and a Cu Kα

source. Data were collected from $2\theta = 5-60°$ at a scan rate of 0.01°/step and 10 s/point. ZP and DLS analyses were performed using a Zetasizer Nano series instrument (Malvern Inst. Ltd., Malvern, UK). EDS analysis was carried out using an SEM JEM-16036 LA instrument integrated with JED-2300 EDX.

Synthesis of the OLA-Capped AuNPs and AgNPs. The plasmonic NPs were synthesized by first capping them with citrate. The citrate-capped AuNPs were synthesized by mixing 1 mL of 1% $HAuCl_4 \cdot 3H_2O$ with 79 mL of water and adding 20 mL of a solution containing 4 mL of 1% tri-sodium citrate with 0.5 mL of tannic acid and 15.5 mL of water.[34] The solution was stirred for several minutes at 60 °C. To form the citrate-capped AgNPs, $HAuCl_4 \cdot 3H_2O$ was replaced with $AgNO_3$, and the rest of the procedure for the citrate-capped AuNPs was followed. A ligand exchange reaction was used to convert the hydrophilic NPs to hydrophobic NPs by replacing the citrate with OLA. First, 2 mL of OLA was mixed with 20 mL of toluene and stirred for few minutes. Then, 50 mL each of the citrate-capped AuNPs and the AgNPs was added to the separate OLA−toluene solutions and stirred until the OLA-capped NPs visibly separated from the hydrophilic layer. The solution was centrifuged, and the top layer containing the OLA-NPs was removed via a pipette.

Synthesis of the Zinc-Blende, Alloyed AuNP-Assisted CdZnSeS QDs. Organometallic hot-injection pyrolysis of the metal precursors was used to fabricate the alloyed QDs using plasmonic NPs as the precursor material (Scheme 1). Both the metal precursors and the OLA-AuNPs precursor were utilized in the same synthetic pot. To synthesize the zinc-blende, alloyed $AuCdZnSeS_{626}$ QDs, 0.4 g of CdO, 1.93 g of TOPO, 1.2 g of HDA, 20 mL of ODE, and 15 mL of OA were stirred and heated up to >200 °C under a constant flow of Ar gas. Then, a premixed TOPS solution containing 80 mg of S, 1.93 g of TOPO, 1 mL of TOP, 10 mL of ODE, and 5 mL of OA was added into the Cd precursor solution and followed by swiftly injecting a premixed TOPZn solution containing 2 mL of Et_2Zn, 1.93 g of TOPO, 1 mL of TOP, 10 mL of ODE, and 5 mL of OA. Next, 5 mL of the OLA-AuNPs and a premixed TOPSe solution (2 mL) containing 60 mg of Se and 5 mL of TOP were added.

To synthesize the zinc-blende, alloyed $AuCdZnSeS_{638}$ QDs and the TOPZn and TOPS precursor solutions were used as described for the $AuCdZnSeS_{626}$ synthesis. Briefly, 0.4 g of CdO, 1.93 g of TOPO, 2 mL of TOP, 5 mL of OLA, 20 mL of ODE, and 15 mL of OA were first stirred and heated up to >200 °C under the constant flow of Ar gas. Then, a premixed TOPSe (5 mL) precursor containing 1.93 g of TOPO, 0.3 g of Se, 20 mL of ODE, and 1 mL of TOP was injected into the Cd precursor and quickly followed by the addition of a premixed TOPZn solution (5 mL), a TOPS solution, and the OLA-AuNPs solution (5 mL).

Synthesis of the Wurtzite, Alloyed AuNP-Assisted CdZnSeS QDs (Scheme 1). To synthesize the alloyed, wurtzite $AuCdZnSeS_{662}$, $AuCdZnSeS_{668}$, and $AuCdZnSeS_{670}$ QDs, the TOPZn and TOPS precursors were used as described for the zinc-blende $AuCdZnSeS_{626}$ QDs, and the TOPSe precursor was used as described for the zinc-blende $AuCdZnSeS_{638}$ QDs. Briefly, 0.4 g of CdO, 3.86 g of TOPO, 2 mL of TOP, 5 mL of TOA, 2 mL of TBP, 20 mL of ODE, and 15 mL of OA were stirred and heated up to >200 °C under a constant flow of Ar gas. Then, the Cd precursor solution became clear, and the TOPSe, TOPZn, TOPS, and OLA-

AuNPs metal precursor solutions were added for nucleation and growth of the alloyed QDs. The alloyed QDs were removed at different time intervals.

Synthesis of the Alloyed AgNP-Assisted CdZnSeS QDs. The synthesis of the alloyed AgCdZnSeS QDs using AgNPs as the precursor material was similar to that of the AuCdZnSeS QDs. The fabrication method used to synthesize the zinc-blende, alloyed $AuCdZnSeS_{638}$ QDs was used to synthesize the alloyed $AgCdZnSeS_{582}$ QDs, and the method used to synthesize the wurtzite AuCdZnSeS QDs was used to synthesize the $AgCdZnSeS_{612}$ and $AgCdZnSeS_{626}$ QDs. OLA-AgNPs was used as the plasmonic NP precursor.

Synthesis of the Alloyed CdZnSeS QDs without a Plasmonic NP Precursor. The fabrication method used to synthesize the alloyed $AuCdZnSeS_{638}$ QDs was employed to synthesize the alloyed CdZnSeS QDs without a plasmonic NP precursor in the growth solution. Three sizes of QDs were removed from the solution at different time intervals.

Ligand Exchange with L-Cysteine. The ligand exchange reaction to replace the organic caps on the alloyed QD surfaces with water-soluble L-cysteine ligand was carried out using an L-cysteine−KOH−methanol−water solution. A KOH−methanol solution was first prepared by dissolving 3.0 g of KOH in 40 mL of methanol, and then, 2.5 g of L-cysteine was added. The mixture was sonicated until the cysteine completely dissolved. Each of the alloyed QDs, with or without a plasmonic precursor, was dissolved in chloroform and added to separate L-cysteine−KOH−methanol solutions. This was followed by the addition of an appropriate volume of water to facilitate an effective precipitation of the water-soluble layer. The solution was stirred for several minutes and allowed to stand overnight so an effective separation of the organic layer from the water-soluble layer could occur. Purification of the nanocrystals was carried out by centrifuging them in acetone and chloroform, and a complete removal of the organic capping was carried out using a chloroform−acetone−water mixture.

■ ASSOCIATED CONTENT

Ⓢ Supporting Information

The Supporting Information is available free of charge on the ACS Publications website at DOI: 10.1021/acsomega.7b01724.

> Details of the PXRD patterns for the L-cysteine-capped CdZnSeS QDs, elemental mapping images of the AuNP and AgNP-assisted alloyed QD synthesis, particle size distribution histogram for AuNP, AgNPs, L-cyst-AuCdZnSeS, and L-cyst-AgCdZnSeS QDs, particle size distribution histogram for the alloyed CdZnSeS QDs, DLS hydrodynamic size distribution and ZP plots of the alloyed L-cyst-AgCdZnSeS QDs and L-cyst-CdZnSeS QDs, and the MTT viability assay of the alloyed L-cyst-CdZnSeS QDs synthesized with or without plasmonic NPs (PDF)

■ AUTHOR INFORMATION

Corresponding Authors

*E-mail: adegoke.sesan@mailbox.co.za (O.A.).
*E-mail: park.enoch@shizuoka.ac.jp (E.Y.P.).

ORCID Ⓞ

Enoch Y. Park: 0000-0002-7840-1424

Notes

The authors declare no competing financial interest.

ACKNOWLEDGMENTS

REFERENCES

(1) Ruberu, T. P. A.; Albright, H. R.; Callis, B.; Ward, B.; Cisneros, J.; Fan, H.-J.; Vela, J. Molecular Control of the Nanoscale: Effect of Phosphine−Chalcogenide Reactivity on CdS−CdSe Nanocrystal Composition and Morphology. *ACS Nano* **2012**, *6*, 5348−5359.

(2) Jang, E.; Jun, S.; Pu, L. High Quality CdSeS Nanocrystals Synthesized by Facile Single Injection Process and their Electroluminescence. *Chem. Commun.* **2003**, 2964−2965.

(3) Aubert, T.; Cirillo, M.; Flamee, S.; Van Deun, R.; Lange, H.; Thomsen, C.; Hens, Z. Homogeneously Alloyed CdSe1-xSx Quantum Dots (0 ≤ x ≤ 1): An Efficient Synthesis for Full Optical Tunability. *Chem. Mater.* **2013**, *25*, 2388−2390.

(4) Ouyang, J.; Vincent, M.; Kingston, D.; Descours, P.; Boivineau, T.; Zaman, B. M.; Wu, X.; Yu, K. Noninjection, One-Pot Synthesis of Photoluminescent Colloidal Homogeneously Alloyed CdSeS Quantum Dots. *J. Phys. Chem. C* **2009**, *113*, 5193−5200.

(5) Deng, Z.; Yan, H.; Liu, Y. Band Gap Engineering of Quaternary-Alloyed ZnCdSSe Quantum Dots via a Facile Phosphine-Free Colloidal Method. *J. Am. Chem. Soc.* **2009**, *131*, 17744−17745.

(6) Xia, X.; Liu, Z.; Du, G.; Li, Y.; Ma, M.; Yao, K. Blue−Green Luminescent CdZnSeS Nanocrystals Synthesized with Activated Alkylthiol. *J. Lumin.* **2012**, *132*, 100−105.

(7) Liu, F.-C.; Cheng, T.-L.; Shen, C.-C.; Tseng, W.-L,.; Chiang, M. Y. Synthesis of Cysteine-Capped ZnxCd1-xSe Alloyed Quantum Dots Emitting in the Blue-Green Spectral Range. *Langmuir* **2008**, *24*, 2162−2167.

(8) Ma, W.; Luther, J. M.; Zheng, H.; Wu, Y.; Alivisatos, A. P. Photovoltaic Devices Employing Ternary PbSxSe1-x Nanocrystals. *Nano Lett.* **2009**, *9*, 1699−1703.

(9) Yang, Z.; Chang, H.-T. CdHgTe and CdTe Quantum Dot Solar Cells Displaying an Energy Conversion Efficiency Exceeding 2%. *Sol. Energy Mater. Sol. Cells* **2010**, *94*, 2046−2051.

(10) Caruge, J. M.; Halpert, J. E.; Wood, V.; Bulović, V.; Bawendi, M. G. Colloidal Quantum-Dot Light-Emitting Diodes with Metal-Oxide Charge Transport Layers. *Nat. Photonics* **2008**, *2*, 247.

(11) Lim, J.; Park, M.; Bae, W. K.; Lee, D.; Lee, S.; Lee, C.; Char, K. Highly Efficient Cadmium-Free Quantum Dot Light-Emitting Diodes Enabled by the Direct Formation of Excitons Within InP@ZnSeS Quantum Dots. *ACS Nano* **2013**, *7*, 9019−9026.

(12) Panda, S. K.; Hickey, S. G.; Waurisch, C.; Eychmüller, A. Gradated Alloyed CdZnSe Nanocrystals with High Luminescence Quantum Yields and Stability for Optoelectronic and Biological Applications. *J. Mater. Chem.* **2011**, *21*, 11550−11555.

(13) Peng, X. Band Gap and Composition Engineering on a Nanocrystal (BCEN) in Solution. *Acc. Chem. Res.* **2010**, *43*, 1387−1395.

(14) Kulakovich, O.; Strekal, N.; Yaroshevich, A.; Maskevich, S.; Gaponenko, S.; Nabiev, I.; Woggon, U.; Artemyev, M. Enhanced Luminescence of CdSe Quantum Dots on Gold Colloids. *Nano Lett.* **2002**, *2*, 1449−1452.

(15) Pompa, P. P.; Martiradonna, L.; Torre, A. D.; Sala, F. D.; Manna, L.; De Vittorio, M.; Calabi, F.; Cingolani, R.; Rinaldi, R. Metal-Enhanced Fluorescence of Colloidal Nanocrystals with Nanoscale Control. *Nat. Nanotechnol.* **2006**, *1*, 126−130.

(16) Shimizu, K. T.; Woo, W. K.; Fisher, B. R.; Eisler, H. J.; Bawendi, M. G. Surface Enhanced Emission from Single Semiconductor Nanocrystals. *Phys. Rev. Lett.* **2002**, *89*, 117401.

(17) Mokari, T. Selective Growth of Metal Tips onto Semiconductor Quantum Rods and Tetrapods. *Science* **2004**, *304*, 1787−1790.

(18) Sun, Z.; Yang, Z.; Zhou, J.; Yeung, M. H.; Ni, W.; Wu, H.; Wang, J. A General Approach to the Synthesis of Gold-Metal Sulfide Core-Shell And Heterostructures. *Angew. Chem., Int. Ed.* **2009**, *48*, 2881−2885.

(19) Kumar, P.; Diab, M.; Flomin, K.; Rukenstein, P.; Mokari, T. Organic Phase Synthesis of Noble Metal-Zinc Chalcogenide Core-Shell Nanostructures. *J. Colloid Interface Sci.* **2016**, *480*, 159−165.

(20) Jin, Y.; Gao, X. Plasmonic Fluorescent Quantum Dots. *Nat. Nanotechnol.* **2009**, *4*, 571−576.

(21) Baer, R.; Neuhauser, D.; Weiss, S. Enhanced Absorption Induced by a Metallic Nanoshell. *Nano Lett.* **2004**, *4*, 85−88.

(22) Samanta, A.; Zhou, Y.; Zou, S.; Yan, H.; Liu, Y. Fluorescence Quenching of Quantum Dots by Gold Nanoparticles: A Potential Long Range Spectroscopic Ruler. *Nano Lett.* **2014**, *14*, 5052−5057.

(23) Gerdes, F.; Navío, C.; Juárez, B. H.; Klinke, C. Size, Shape, and Phase Control in Ultrathin CdSe Nanosheets. *Nano Lett.* **2017**, *17*, 4165−4171.

(24) Li, Z.; Peng, X. Size/Shape-Controlled Synthesis of Colloidal CdSe Quantum Disks: Ligand and Temperature Effects. *J. Am. Chem. Soc.* **2011**, *133*, 6578−6586.

(25) Chin, P. T. K.; Donegá, C. d. M.; van Bavel, S. S.; Meskers, S. C. J.; Sommerdijk, N. A. J. M.; Janssen, R. A. J. Highly Luminescent CdTe/CdSe Colloidal Heteronanocrystals with Temperature-Dependent Emission Colour. *J. Am. Chem. Soc.* **2007**, *129*, 14880−14886.

(26) Kubin, R. F.; Fletcher, A. N. Fluorescence Quantum Yields of Some Rhodamine Dyes. *J. Lumin.* **1982**, *27*, 455−462.

(27) Mosmann, T. Rapid Colorimetric Assay for Cellular Growth and Survival: Application to Proliferation and Cytotoxicity Assays. *J. Immunol. Methods* **1983**, *65*, 55−63.

(28) Adegoke, O.; Park, E. Y. Nanofabricated Optical Tuning and Epitaxial Overgrowth of In2S3 Shells on CdSe Cores. *New J. Chem.* **2017**, *41*, 1303−1312.

(29) Thanh, N. T. K.; Maclean, N.; Mahiddine, S. Mechanisms of Nucleation and Growth of Nanoparticles in Solution. *Chem. Rev.* **2014**, *114*, 7610−7630.

(30) Sugimoto, T.; Shiba, F.; Sekiguchi, T.; Itoh, H. Spontaneous Nucleation of Monodisperse Silver Halide Particles from Homogeneous Gelatin Solution I: Silver Chloride. *Colloids Surf., A* **2000**, *164*, 183−203.

(31) Lee, W.-r.; Kim, M. G.; Choi, J.-r.; Park, J.-I.; Ko, S. J.; Oh, S. J.; Cheon, J. Redox-transmetalation Process as a Generalized Synthetic Strategy for Core-shell Magnetic Nanoparticles. *J. Am. Chem. Soc.* **2005**, *127*, 16090−16097.

(32) Owen, J. S.; Chan, E. M.; Liu, H.; Alivisatos, A. P. Precursor Conversion Kinetics and the Nucleation of Cadmium Selenide Nanocrystals. *J. Am. Chem. Soc.* **2010**, *132*, 18206−18213.

(33) Jin, Y.; Gao, X. Plasmonic Fluorescent Quantum Dots. *Nat. Nanotechnol.* **2009**, *4*, 571−576.

(34) Slot, J. W.; Gueza, H. J.; Weerkamp, A. J. Localization of Macromolecular Components by Application of the Immunogold Technique on Cryosectioned Bacteria. *Methods Microbiol.* **1988**, *20*, 211−236.